Science and Technology Facilities Council

Technical Report
STFC-TR-2025-002

Development of Subchannel CFD for Prismatic HTGR Fuel Assemblies

B Liu, C Moulinec, S Rolfo, M Samler, E Iyamabo, M Chevalier

February 2025

Enquiries concerning this report should be addressed to:

RAL Library
STFC Rutherford Appleton Laboratory
Harwell Oxford
Didcot
OX11 0QX

Tel: +44(0)1235 445577
email: library@stfc.ac.uk

Science and Technology Facilities Council reports are available online at:
https://epubs.stfc.ac.uk

Accessibility: a Microsoft Word version of this document (for use with assistive technology) may be available on request.

DOI: 10.5286/stfctr.2025002

ISSN 2753-5797

STFC Author Identifiers (ORCIDs)

Author ORCIDs are provided where available.

Bo Liu	0000-0002-6840-041X
Charles Moulinec	0009-0003-7011-7327
Stefano Rolfo	0000-0001-6325-7629
Marion Samler	0000-0002-4767-5342

Development of Subchannel CFD for Prismatic HTGR Fuel Assemblies

Bo Liu
STFC Daresbury Laboratory
bo.liu@stfc.ac.uk
STFC collaborators: Charles Moulinec, Stefano Rolfo and Marion Samler
EDF Energy collaborators: Ehimen Iyamabo and Marc Chevalier

16 January, 2024

Abstract

This work presents a coarse-grid Computational Fluid Dynamics (CFD) approach, initially developed for light-water reactors and now extended to prismatic High-Temperature Gas-cooled Reactor (HTGR) fuel assemblies. This method, known as Subchannel CFD (SubChCFD), combines the strengths of traditional subchannel codes and CFD. It offers CFD-like 3-D predictions while ensuring integral consistency of the results with well-calibrated empirical correlations. The use of a coarse mesh results in a substantial reduction in computational costs by up to 1 to 3 orders of magnitude compared to conventional CFD, depending on the turbulence model used. This potentially enables cost-effective simulations to be carried out at the reactor core scale. To validate the expanded capability of SubChCFD, the modular HTGR fuel assembly designed by General Atomics is selected for case study. Simulation results demonstrate that SubChCFD aligns well with conventional Reynolds-Averaged Navier-Stokes approaches at a significantly lower computing cost.

Key words: Computational Fluid Dynamics; Subchannel, Coarse mesh; High Temperature Gas-cooled Reactor

Contents

1 Introduction

The High-Temperature Gas-Cooled Reactor (HTGR), a proposed Generation IV nuclear reactor, is gaining increasing attention due to its inherent safety, high thermal efficiency, and capability to generate high-temperature process heat. In 2022, the UK government selected HTGR for a development programme with the objective of having a demonstrator operational by the early 2030s [1]. The successful deployment of HTGR technology requires an in-depth understanding of its reactor physics, particularly the dynamics of coolant flow and heat transfer within the fuel assemblies in the core, and their impacts on the reactor efficiency and structural integrity. This relies on thermal-hydraulic analyses of the reactor system, which is traditionally performed using 0D/1D approaches. With the recent advancement in computing capacity, more advanced Computational Fluid Dynamics (CFD) tools have started to play some role, exhibiting better features than traditional approaches. CFD can provide detailed 3-D predictions of the thermal-hydraulic behaviours of the reactor. However, the substantial requirements on computing resources pose significant challenges to use CFD in real-world engineering applications.

In this study, our objective is to extend a coarse-grid CFD approach, initially developed for light-water reactors, to prismatic HTGRs. This method, referred to as Subchannel CFD (SubChCFD) [2], combines the advantages of traditional subchannel codes and CFD. SubChCFD offers CFD-like 3-D predictions of flow and thermal fields while ensuring integral consistency of the results with well-calibrated empirical correlations, as the correlations are used in the closure modelling of the governing equation system for wall friction and heat transfer calculations. Thanks to the use of a very coarse mesh, the computing cost can be reduced by up to 1 to 3 orders of magnitude compared to the conventional Reynolds Averaged Navier-Stokes (RANS) approach, depending on the turbulence model used. This potentially enables cost-effective simulations to be carried out at the reactor core scale.

HTGRs are helium-cooled thermal neutron reactors with graphite used as both the neutron moderator and reflector. TRISO particles are dispersed within the graphite matrix to create fuel compacts, which are typically cylindrical in shape and inserted into hexagonal graphite blocks. There are two main types of prismatic HTGR fuel designs: pin-in-block and multi-hole. In the pin-in-block design, the diameter of the fuel compact is deliberately designed to be smaller than the fuel holes in the graphite, creating an annular gap between the fuel and the graphite moderator. The gap serves as a coolant channel, allowing helium to flow through and extract heat from the fission reactions. An example of the pin-in-block design is Japan's 30 MW High Temperature Engineering Test Reactor (HTTR) [3]. The multi-hole type of fuel is designed differently, with separate circular coolant channels surrounded by fuel compact holes. Notable examples include designs from General Atomics GT-MHR and its variants (PM600, PM200, MHTGR-350 benchmark) [4, 5], as well as the micro-modular HTR U-Battery [6]. Figure 1 illustrates the distinctions between the two types of fuel designs in prismatic HTGRs.

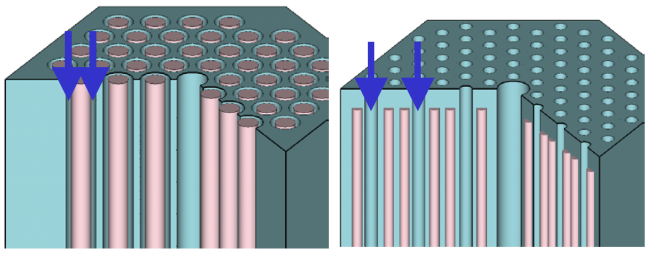

(a) Pin-in-block fuel (b) Multi-hole fuel

Figure 1: Fuel types of prismatic HTGRs.[7]

As previously mentioned, the core concept of the SubChCFD methodology lies in the use of empirical correlations as substitutes for wall functions in the closure of the governing equations solved on the coarse grid. Consequently, the accuracy achievable in a SubChCFD simulation is highly dependent on the choice of the empirical correlations. In the context of a prismatic

HTGR, regardless of whether it adopts the pin-in-block or multi-hole fuel designs, the annular or circular channels through which the coolant circulates naturally become the "subchannels" to be considered in SubChCFD. These subchannels are simple in terms of shape when compared to light-water reactors, making it easier to identify and implement well-validated correlations and consequently enhancing the accuracy of the simulations.

In contrast to light-water reactors, where the main calculation effort focuses on the coolant-side heat transfer, predicting heat conduction within the graphite solid is crucial to the understanding of the thermal-hydraulic behaviours of prismatic HTGRs. This significance arises from the non-uniform distribution of heating power within the fuel compacts and the asymmetry of heat conduction in the graphite blocks. To address these challenges, it is required for SubChCFD to have the capability to handle conjugate heat transfer between the coolant channel and the graphite block. This is essential for providing accurate predictions of fuel temperature, a critical factor in ensuring safe operation of HTGRs.

To sum up, the development objectives for extending SubChCFD to prismatic HTGRs can be outlined as follows:

- Design a dual-mesh system tailored for the specific geometry of the fuel type considered.
- Identify and implement suitable empirical correlations based on the geometric shapes of the coolant subchannels.
- Enable the capability of fluid-solid conjugate heat transfer within the SubChCFD framework.

In this study, we select the multi-hole fuel type to showcase the newly developed capabilities of SubChCFD, as it has been used in most of the latest HTGR fuel designs. The associated methodologies implemented can be easily adapted to accommodate the use of SubChCFD for the pin-in-block fuel type.

2 Methodology

2.1 Overview of SubChCFD

SubChCFD employs a hybrid methodology that combines the characteristics of traditional subchannel analysis tools and modern CFD. In this approach, a dual mesh system is used, comprising (i) a subchannel filtering mesh, which aligns the mesh of typical subchannel codes, allowing the subchannel-level wall friction and heat transfer to be calculated based on well-validated engineering correlations, and (ii) a coarse-grid computing mesh, derived by subdividing the filtering mesh, on which the 3-D RANS governing equations are solved. Typically, the computing mesh consists of $\sim O(10)$ cells within the cross-section of an individual subchannel, so it remains very coarse in comparison to CFD standards.

Figure 2 shows the dual-mesh system used for a typical square Pressurised Water Reactor (PWR) rod bundle [8], illustrating the roles of the computing and subchannel filtering meshes and the interactions between them. It is clear that the computing mesh is completely unstructured and a unstructured CFD solver is used in line with this, providing an advantage in representing the geometrical curvatures of the fuel pins. At each time step of the simulation, the coarse-grid CFD results are averaged over the filtering mesh to derive bulk flow parameters such as subchannel bulk velocity, temperature and fluid thermal physical properties, which are used to derive empirical friction factor and Nusselt number to compute wall friction and heat transfer. The computed values act in turn as boundary conditions for the CFD system of the following time step. The process is performed iteratively until convergence is reached. For transient problems, the calculation loop is conducted based on sub-iterations within the time step to ensure temporal accuracy of the simulation. Differing from subchannel code strategy, such an approach allows flow physics to be resolved up to the computing mesh density while ensuring that the integral effects of the flow align with the predictions of the chosen engineering correlations.

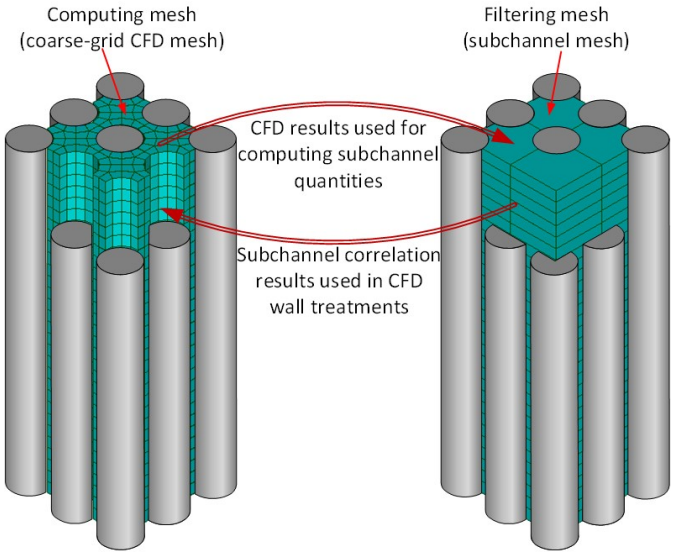

Figure 2: Dual mesh system for a square lattice PWR rod bundle.[8]

2.2 Design of the dual-mesh system

The MHTGR-350 benchmark, a representative prismatic HTGR designed by General Atomics, is used in this study to showcase the design of the dual-mesh system within SubChCFD. Figure 3 provides a cross-sectional view of a standard fuel assembly in the case of MHTGR-350 benchmark. The assembly comprises 210 blind holes for fuel compacts, 108 helium coolant channels (comprising 102 standard channels and 6 small-diameter channels near the centre of the graphite block), and 6 burnable poison rods situated at the corners of the hexagonal graphite block. For simplicity, the burnable poison rods are assumed to have the same thermal-physical properties as graphite, allowing them to be modelled as the latter.

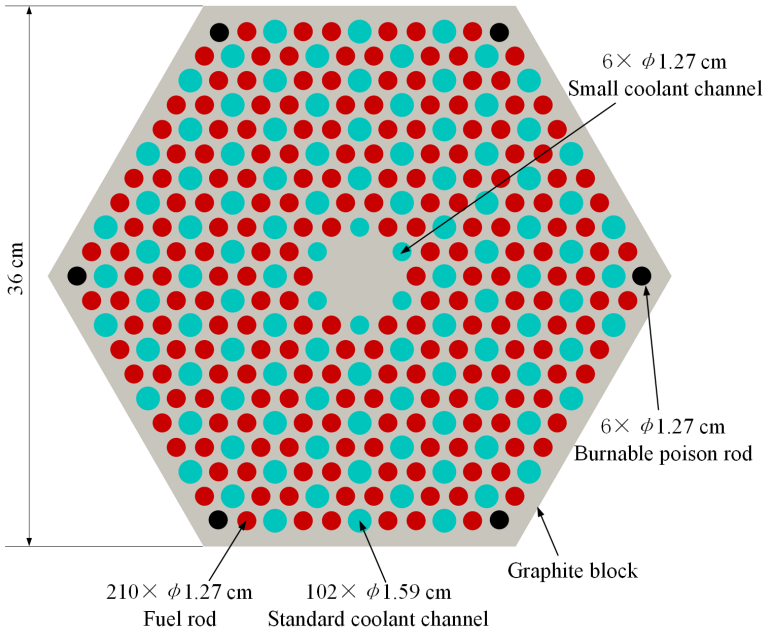

Figure 3: Cross-sectional view of the standard fuel assembly in MHTGR-350 benchmark designed by General Atomics with dimensions.

In the modelling of an HTGR fuel assembly using conventional CFD approaches, highly dense

meshes are often required, particularly in the near-wall regions of the coolant channels. This is essential for capturing the sharp gradients of field variables, leading to a substantial demand for computational resources. In contrast, gradients within the solid materials are generally expected to be much smaller compared to those in the coolant channels. Therefore, there is no need to use fine meshes to address heat conduction within the solid. Instead, relatively coarse meshes can often yield satisfactory predictions. In order to effectively reduce computational costs, the design of the SubChCFD computing mesh is geared towards using coarse meshes for the coolant channels as well, maintaining a cell density comparable to that used for the graphite solid.

Considering the repetitive spatial patterns within the fuel assembly due to symmetries of the hexagonal configurations, a mesh generation strategy, proven successful for light-water reactor applications, is applied in this study. This involves the following steps: (i) identifying the smallest repetitive geometric patterns in the selected HTGR fuel assembly, (ii) generating sub-mesh for each of these patterns individually, (iii) duplicating, translating/rotating, and combining these sub-meshes to create the final mesh for the entire fuel assembly. Figure 4 shows the sub-mesh for each of the repetitive patterns. It can be noted that the same computing mesh is used for fuel compact holes and small coolant channels, featuring radial two-layer cells for the circular holes/channels and single-layer cells for the surrounding graphite. For the standard coolant channels, a radial three-layer mesh is used for the circular channel, while the surrounding graphite is represented with a single-layer mesh. For the remaining graphite solid, repetitive patterns are further categorised into centre, edge, and corner configurations, each with mesh designs depicted at the bottom of Figure 4 (refer to sub-figures (a), (b), and (c)). Figure 5 (a) shows the computing mesh for the entire cross section of the fuel assembly, constructed using the mesh segments presented in Figure 4.

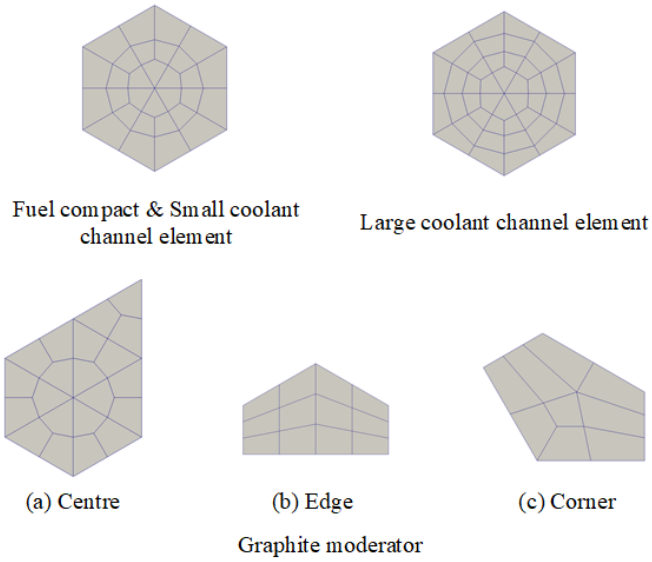

Figure 4: Mesh elements.

In contrast to light-water reactors, the design of the subchannel filtering mesh for HTGRs is inherently not unique. The key factor is to ensure the one-to-one correspondence between each coolant channel and the subchannel mesh element at any axial location. In this study, we choose a strategy of using hybrid triangular-quadrangular elements for the subchannel filtering mesh, as described in Figure 5 (b). It can be noted that the mesh contains empty cells that do not correspond to any coolant channels. Identification of these empty cells is performed during preprocessing, leading to their exclusion from the numbering system and thereby being blocked out from the calculation loops performed over the subchannel filtering mesh.

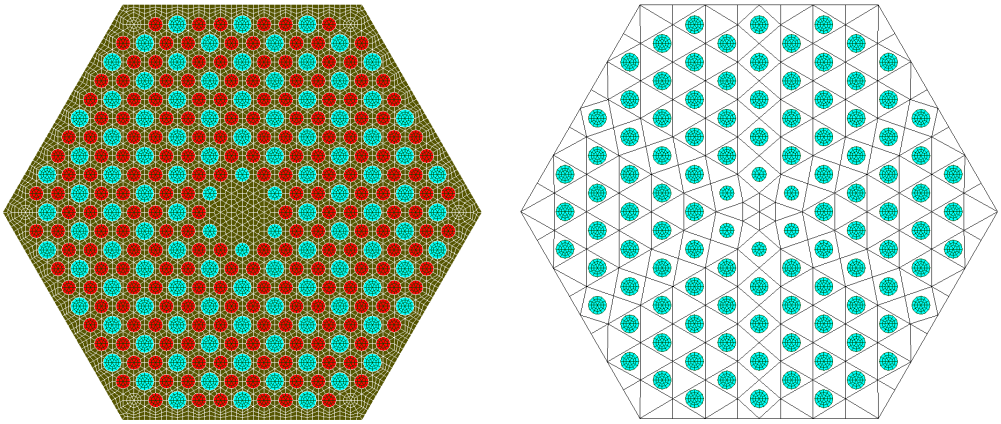

(a) coarse-grid computing mesh (b) Subchannel filtering mesh

Figure 5: Dual mesh system.

2.3 Closure modelling of the momentum equation

We consider the integral form of the RANS momentum equation on a finite volume Ω with a collocated arrangement of the velocity components:

$$\frac{\rho V_\Omega}{\Delta t}(\mathbf{U}^{n+1}-\mathbf{U}^n)+\oint_S \mathbf{U}^{n+1}(\mathbf{J}^n\cdot\mathbf{n})\,dS=-\oint_S(\bar{\bar{I}}p\cdot\mathbf{n})\,dS+\oint_S(\bar{\bar{\sigma}}^{n+1}\cdot\mathbf{n})\,dS+V_\Omega S_M \tag{1}$$

where ρ is the fluid density, $\mathbf{U}$ is the velocity vector, V_Ω denotes the volume of the computing mesh cell Ω, Δt is the time step, and the superscripts n and $n+1$ correspond to the n^{th} and $(n+1)^{th}$ time steps, respectively. $\mathbf{J}=\rho\mathbf{U}$ represents the convective mass flux, $\mathbf{n}$ is the unit normal vector, S denotes the area of the cell surface, $\bar{\bar{I}}$ and $\bar{\bar{\sigma}}$ stand for the unit tensor and the stress tensor, respectively. S_M represents a general source term. To ensure the pressure drop in the coolant channel to be consistent with empirical correlations, the integral diffusion term in Equation 1 for the wall-adjacent cells is decomposed into an interior-surface term and a wall-surface term:

$$\oint_S(\bar{\bar{\sigma}}^{n+1}\cdot\mathbf{n})\,dS=\underbrace{\int_{S_i}(\bar{\bar{\sigma}}^{n+1}\cdot\mathbf{n})\,dS}_{\text{interior-surface}}+\underbrace{\int_{S_b}(\bar{\bar{\sigma}}^{n+1}\cdot\mathbf{n})\,dS}_{\text{wall-surface}} \tag{2}$$

The interior-surface term is treated using a standard RANS approach as follows:

$$\int_{S_i}(\bar{\bar{\sigma}}^{n+1}\cdot\mathbf{n})\,dS=\int_{S_i}(\mu+\mu_t)[\nabla\mathbf{U}+(\nabla\mathbf{U})^T-\frac{2}{3}\delta\nabla\cdot\mathbf{U}]\cdot\mathbf{n}\,dS \tag{3}$$

Here, μ is the molecular viscosity, δ is the kronecker delta, μ_t is the eddy viscosity, modelled using low-order turbulence models, such as the mixing length model, considering that the interior surfaces of the computing cells are situated at a significant distance away from walls, because of the large cell sizes. Consequently, these surfaces can be safely assumed to be located within fully turbulent regions, where simple turbulence models are expected to produce satisfactory predictions of the overall turbulence. The wall-surface term, on the contrary, is modelled with the information of bulk flow and empiricism-based friction factors:

$$\int_{S_b}(\bar{\bar{\sigma}}^{n+1}\cdot\mathbf{n})\,dS=-\frac{1}{2}f\rho_{sub}\mathbf{U_{sub}}|\mathbf{U_{sub}}|\int_{S_b}dS \tag{4}$$

where ρ_{sub} and $\mathbf{U_{sub}}$ represent the subchannel bulk density and velocity, respectively. In the present work, the Darcy friction factor $C_f=4f$ is given by the correlation [9] shown in Equation 5,

$$C_f = \begin{cases} \dfrac{64}{\mathbf{Re}} & \mathbf{Re} < 2300 \\ 0.316\mathbf{Re}^{-\frac{1}{4}} & 2300 \leq \mathbf{Re} < 3 \times 10^4 \text{ (Blasius)} \\ 0.184\mathbf{Re}^{-\frac{1}{5}} & 3 \times 10^4 \leq \mathbf{Re} < 10^6 \text{ (McAdams)} \end{cases} \tag{5}$$

2.4 Conjugate heat transfer

Achieving accurate prediction of the thermal behaviour of HTGR fuel assemblies requires accounting for heat conduction within the solid. Consequently, numerical modelling must address the conjugate heat transfer (CHT) between the coolant channels and the graphite blocks. However, the current version of SubChCFD lacks this crucial functionality, so enabling CHT with SubChCFD is a primary focus of this work. Broadly, there are two approaches to implement CHT in SubChCFD:

(1) **Coupling SubChCFD with an external solid software.** Given the fact that SubChCFD has been well validated under prescribed heat flux boundary conditions, a Neumann/Robin boundary pair can be employed to couple the fluid and solid solvers at the interfaces. Specifically, a Robin-type boundary condition can be applied on the solid side, with the bulk ambient fluid temperature and heat transfer coefficient[1] determined using the results from the fluid side solutions and a chosen Nusselt number correlation. Simultaneously, a Neumann-type boundary condition can be implemented on the fluid side, with wall heat fluxes obtained from the solutions of the thermal field of the solid. This method minimises the needs for necessary modifications in the existing mathematical framework of SubChCFD, but the convergence efficiency is expected to be limited due to the explicit nature of the coupling.

(2) **Coupling within a single CFD solver.** This approach entails solving the energy equation for both the fluid and solid within a unified matrix system, so the coupling is implicit and strong. As sub-iterations are not needed between the fluid and solid sub-domains, this method is anticipated to be more stable and efficient than method (1). To make it workable with SubChCFD, effective thermal exchange coefficients need to be implemented to the wall adjacent fluid cells, to ensure correct heat fluxes through the fluid-solid interfaces. These coefficients should be calculated based on the Nusselt number correlation used, which is described in detail in the rest of this section.

Figure 6 shows a sketch of cells of arbitrary shapes at the two sides of a fluid-solid interface.

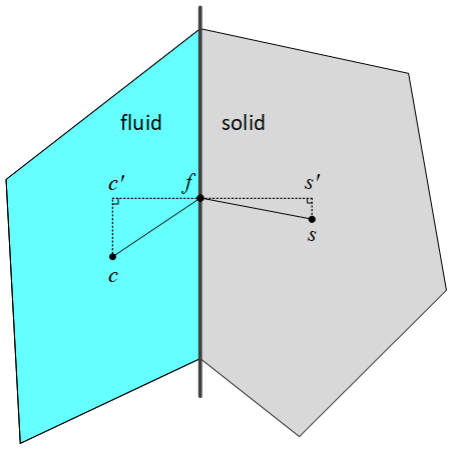

Figure 6: Computing cells near the fluid-solid interface.

Based on the conservation of heat flux through the interface, the following equation holds,

[1] $h = Nu \cdot \lambda / L$, where Nu is the Nusselt number, λ is the thermal conductivity of the coolant, and L is the length scale - the hydraulic diameter of the of coolant channel in this case.

$$q_f = \lambda_s \frac{T_{s'} - T_f}{|x_f - x_{s'}|} = \lambda_c^{eff} \frac{T_f - T_{c'}}{|x_f - x_{c'}|} \tag{6}$$

where q_f is the heat flux through the interface f, T_i and x_i are the temperature and spatial coordinate at location i, λ_s is the thermal conductivity of the solid cell, and λ_c^{eff} is the effective thermal conductivity of the fluid cell. We further define the external and internal exchange coefficients as

$$h_{ext} = \frac{\lambda_s}{|x_f - x_{s'}|} \tag{7}$$

and

$$h_{int} = \frac{\lambda_c^{eff}}{|x_f - x_{c'}|} \tag{8}$$

Then, Equation 6 can be rewritten as follows,

$$\begin{cases} h_{ext}(T_{s'} - T_f) = q_f \\ h_{int}(T_f - T_{c'}) = q_f \\ h_{sub}(T_f - T_{sub}) = q_f \end{cases} \tag{9}$$

It can be noted that a third equation is introduced based on the subchannel mean heat transfer coefficient h_{sub} and subchannel bulk fluid temperature T_{sub}. Consequently, there are three equations with three unknowns, namely T_f, q_f, and h_{int} (since λ_c^{eff} is unknown). The internal thermal exchange coefficient h_{int} can then be determined as follows,

$$\begin{cases} T_f = \dfrac{h_{ext} T_{s'} + h_{sub} T_{sub}}{h_{sub} + h_{ext}} \\ q_f = h_{ext}(T_{s'} - T_f) \\ h_{int} = \dfrac{q_f}{T_f - T_{c'}} \end{cases} \tag{10}$$

where $h_{sub} = Nu \cdot \lambda / D_h$ is calculated based the following Nusselt number correlation,

$$\mathbf{Nu} = \begin{cases} 4.36 & \mathbf{Re} < 2300 \\ 0.021\mathbf{Re}^{0.8}\mathbf{Pr}^{0.4} & \mathbf{Re} \geq 2300 \text{ (heating)} \\ 0.021\mathbf{Re}^{0.8}\mathbf{Pr}^{0.3} & \mathbf{Re} \geq 2300 \text{ (cooling)} \end{cases} \tag{11}$$

In this work, we decide to choose method (2) to implement the CHT capability in SubChCFD. This choice is facilitated by the "internal coupling" functionality provided by *code_saturne*, the CFD platform on which SubChCFD is implemented. This functionality allows for the implicit solution of a scalar equation over both the fluid and solid domains. The internal exchange coefficient of the wall-adjacent fluid cell is replaced by the result given by Equation 10, so that the heat flux through the interface aligns with the Nusselt number correlation used.

3 Case studies

3.1 Simulation of an axially fully developed flow

The new development is first assessed using a postulated fully developed flow in a fuel assembly of the MHTGR-350 benchmark with CHT considered. The SubChCFD model is created based on the complete cross-section of the fuel assembly, with only one layer of mesh in the axial direction. The computing mesh adheres to the meshing strategy illustrated in Figure 4, resulting in a total mesh size of 11,844 cells. Additionally, RANS simulations are conducted for the same flow condition to provide reference results. Figure 7 shows the mesh used for the RANS model, generated for a 1/12 sector of the fuel assembly, yielding a total mesh size of 28,788 (30 times larger than the coarse mesh when based on the same geometry). A detailed comparison of the

meshes used in the RANS model and the SubChCFD model is also presented in Figure 7. It can be seen that the mesh used in the RANS model has a significantly higher cell density than that used in SubChCFD, particularly in the near-wall regions of the coolant channels. This justifies the use of a wall-resolved turbulence model (the k-ω SST model), allowing for the continuous solution of governing equations down to the viscous sublayer ($y^+ \sim 5$).

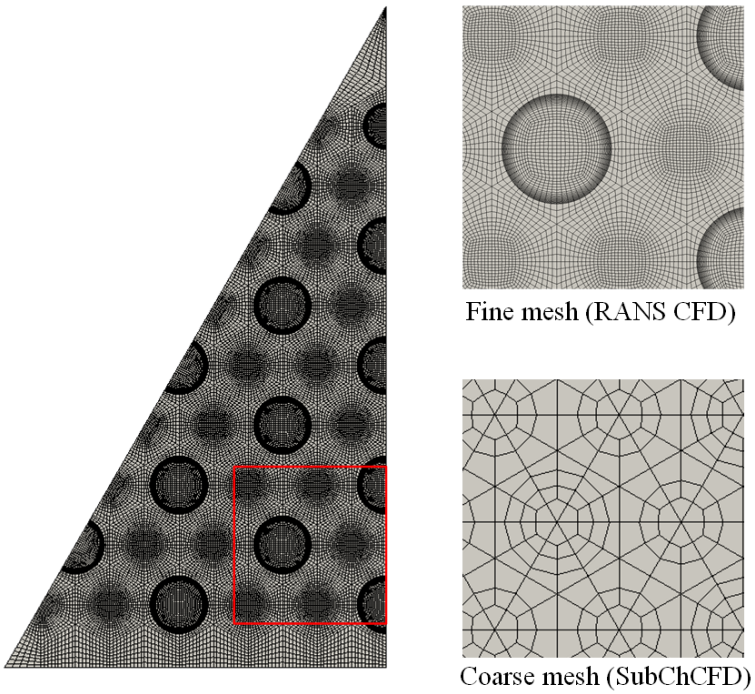

Figure 7: Meshes.

A constant momentum source term, representing the axial pressure gradient, is applied to the coolant channels to provide an axial driving force for the flow. The magnitude of the momentum source is automatically adjusted throughout the simulation until a steady state is reached, to ensure the mass flow rate is kept at 0.235 kg/s (based on the 1/12 sector). A uniform heating power of 31.1 MW/m^3 is imposed on the fuel compacts, aligning with the nominal design conditions of the MHTGR-350 reactor. To achieve steady-state temperature distributions in the simulation, an energy sink is introduced to the energy equation and applied to the coolant channels to remove the bulk temperature increase within the computational domain. Based on the physical nature of the thermal periodicity, the energy sink is not constant and its distribution can be expressed as follows,

$$S_E = -\frac{\dot{Q} U_z}{\int_\Omega U_z \, dV} \tag{12}$$

where $\dot{Q}$ is the net heat input, U_z is the cell velocity, and Ω represents the fluid domain. The distribution of the energy source term, encompassing positive values on the fuel and negative values on the coolant, across the 1/12 sector of the fuel assembly is presented in Figure 8. To be consistent with the periodicity assumption, all thermal physical properties of the helium coolant and solid materials (fuel compact and graphite) are assumed to be constant, based on the design temperature of 950 °C at the coolant outlet.

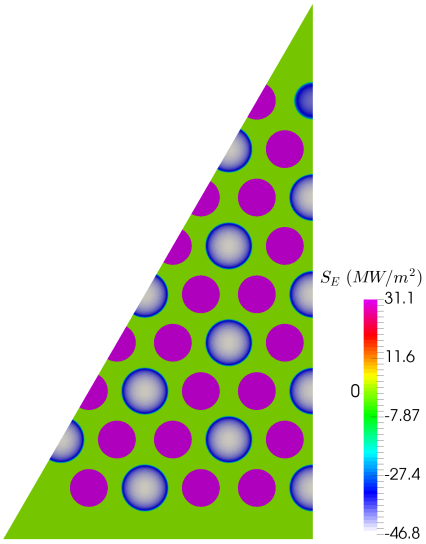

Figure 8: Distribution of the energy source/sink in the 1/12 sector of the fuel assembly.

When a coarse mesh is used, noticeable discrepancies may emerge between the mesh and the original geometry due to the linear approximation of curvature. For instance, representing a circular channel with an inscribed polygon (in the present case, a dodecagon) may lead to a reduction in channel cross-sectional area, potentially resulting in an overestimation of the coolant velocity for a given mass flow rate. The reduction is negligible if the mesh is circumferentially fine, but it can be as high as 4% with the coarse mesh used in this research. A practical solution is to implement a correction to the geometry to counteract such reduction, achieved by slightly enlarging the diameter of the coolant channel and the fuel compact. Figure 9 provides a comparison of the coolant channel before and after correction, demonstrating a 4% enlargement of the corrected coolant channel to maintain consistency in the cross-sectional area with the original geometry. A similar adjustment is applied to the fuel compact to ensure the heating power is correctly imposed.

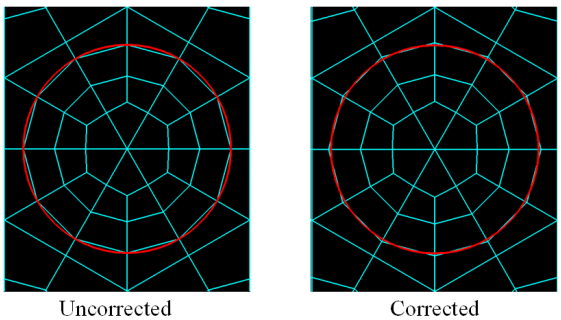

Figure 9: Geometrical correction in the coarse-grid model.

Figure 10 shows the pressure drop results obtained from the simulations. The empirical correlation employed in SubChCFD demonstrates excellent prediction in accurately reproducing wall shears, exhibiting only a 2.6% difference in pressure drop prediction compared to the RANS model. Additionally, the same coarse mesh is used to perform RANS simulation with a standard wall function approach. The results reveal that the wall function does not perform as effectively as the empirical correlation for fully developed flows on a coarse mesh, despite the y^+ of the first cell falling within the valid range of the log law for the considered flow condition. This is because the wall function links the wall shear stress locally to the velocity of the first cell, and the latter cannot be accurately predicted due to the relatively large truncation error introduced by the coarse mesh. In contrast, SubChCFD directly links the wall shear stress to the subchannel

bulk velocity, which is accurately enforced under a finite volume CFD framework because of the imposed mass conservation.

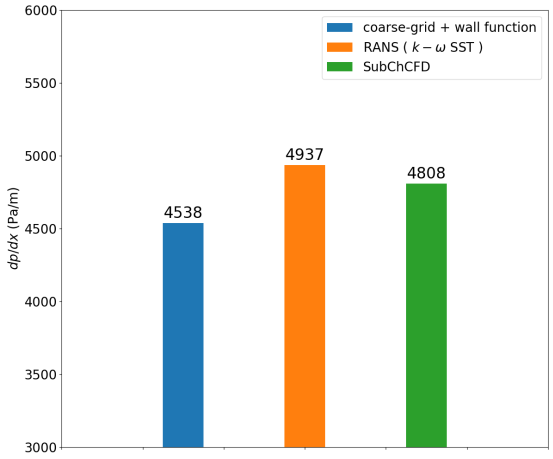

Figure 10: Axial pressure drop.

The temperature distributions are presented in Figure 11. For a direct comparison of the results, the RANS result (originally available for only the 1/12 sector) is duplicated and further combined to reconstruct the entire sector, leveraging the symmetries inherent to the problem. The overall patterns of the temperature contours predicted by RANS and SubChCFD models exhibit good agreement. The highest solid temperature is observed at the first rank of the fuel compacts near the centre of the fuel block. SubChCFD provides a slightly lower prediction of the peak temperature compared to the RANS predictions for these areas. Accordingly, the coolant temperature also peaks at the first rank of coolant channels and gradually decreases away from the centre of the fuel block, attaining its minimum at the peripheral channels.

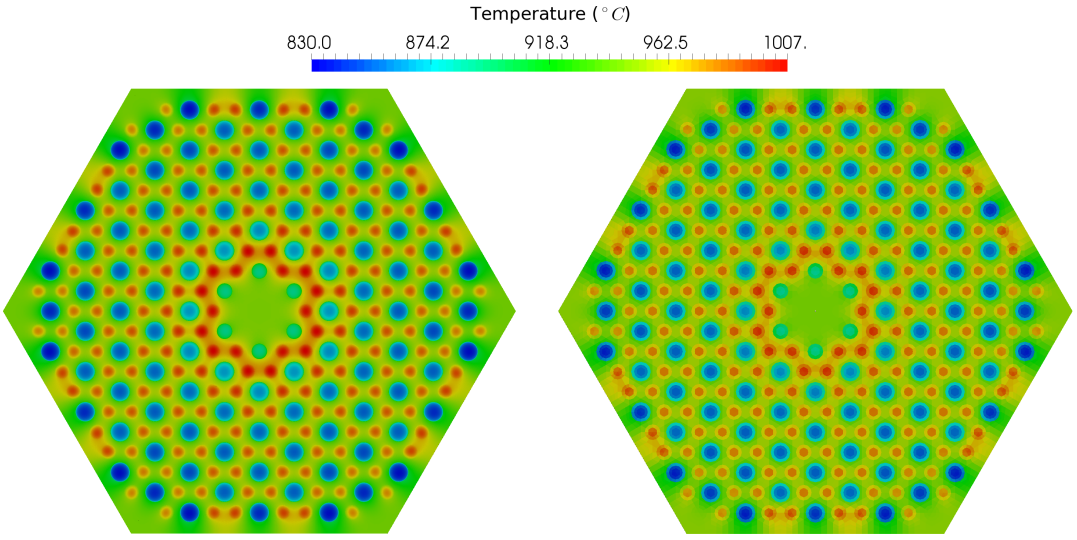

Figure 11: Comparison of temperature contours between RANS and SubChCFD.

For a more detailed investigation of the heat transfer from the fuel to the coolant, the coolant channels are numbered as shown in Figure 12. The channel bulk temperature and Nusselt number are then calculated for each individual coolant channel and presented in Figures 13 and 14, respectively. Notably, SubChCFD closely predicts the coolant channel bulk temperatures in comparison to those obtained from the RANS model. The maximum difference between the two is only 3.5 °C, occurring in the coolant channels near the centre of the fuel block (channels

No. 1, 2, and 3). Similarly, the predicted channel mean Nusselt numbers also exhibit good agreement. It is important to highlight that the elevated coolant temperature in the first-rank channels results from a relatively low Nusselt number, indicating a reduction in coolability. This, in turn, contributes to the elevated fuel temperature in the adjacent regions.

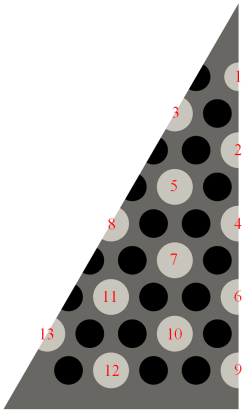

Figure 12: Numbering of the coolant channels.

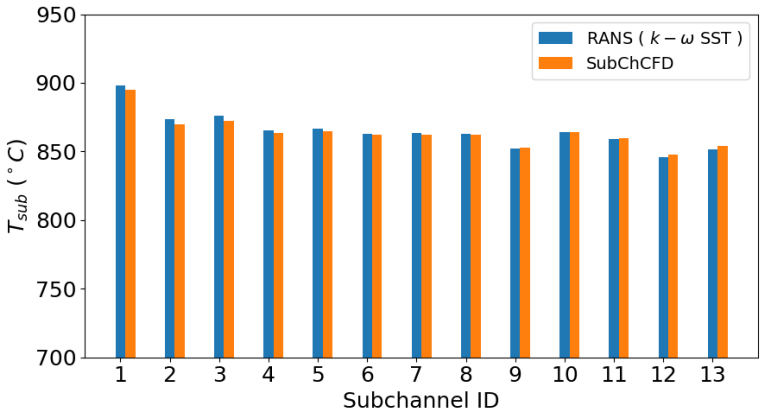

Figure 13: Coolant channel bulk temperature.

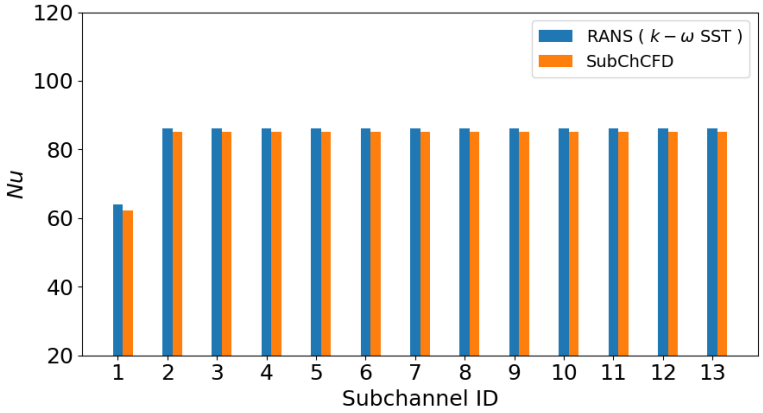

Figure 14: Coolant channel mean Nusselt number.

Figure 15 shows the circumferential distribution of the surface heat fluxes of the selected

coolant channels. They can be categorised into three groups based on the magnitude of the circumferential heat flux variation: the centre (channels 1, 2 and 3), intermediate (channels 4, 5, 6 7, 8 and 11), and peripheral (channels 9, 10, 12 and 13) channels. In the centre and peripheral channels, heat fluxes exhibit significant variations along the circumferential direction due to the asymmetrical arrangement of the surrounding fuel compacts. Higher heat flux is anticipated at locations where fuel compacts are installed compared to locations without them. The large scale variations are well captured by both the RANS and SubChCFD models, whereas some details are not as pronounced in the SubChCFD predictions, owing to the use of a coarse mesh that lacks sufficient spatial resolution to resolve such details. In the intermediate channels, on the other hand, the heat fluxes tend to be more uniformly distributed. Again, details are well captured by the RANS model, while SubChCFD provides relatively flat predictions with fewer details. Nevertheless, the overall magnitudes in SubChCFD align well with those from the RANS model in all cases.

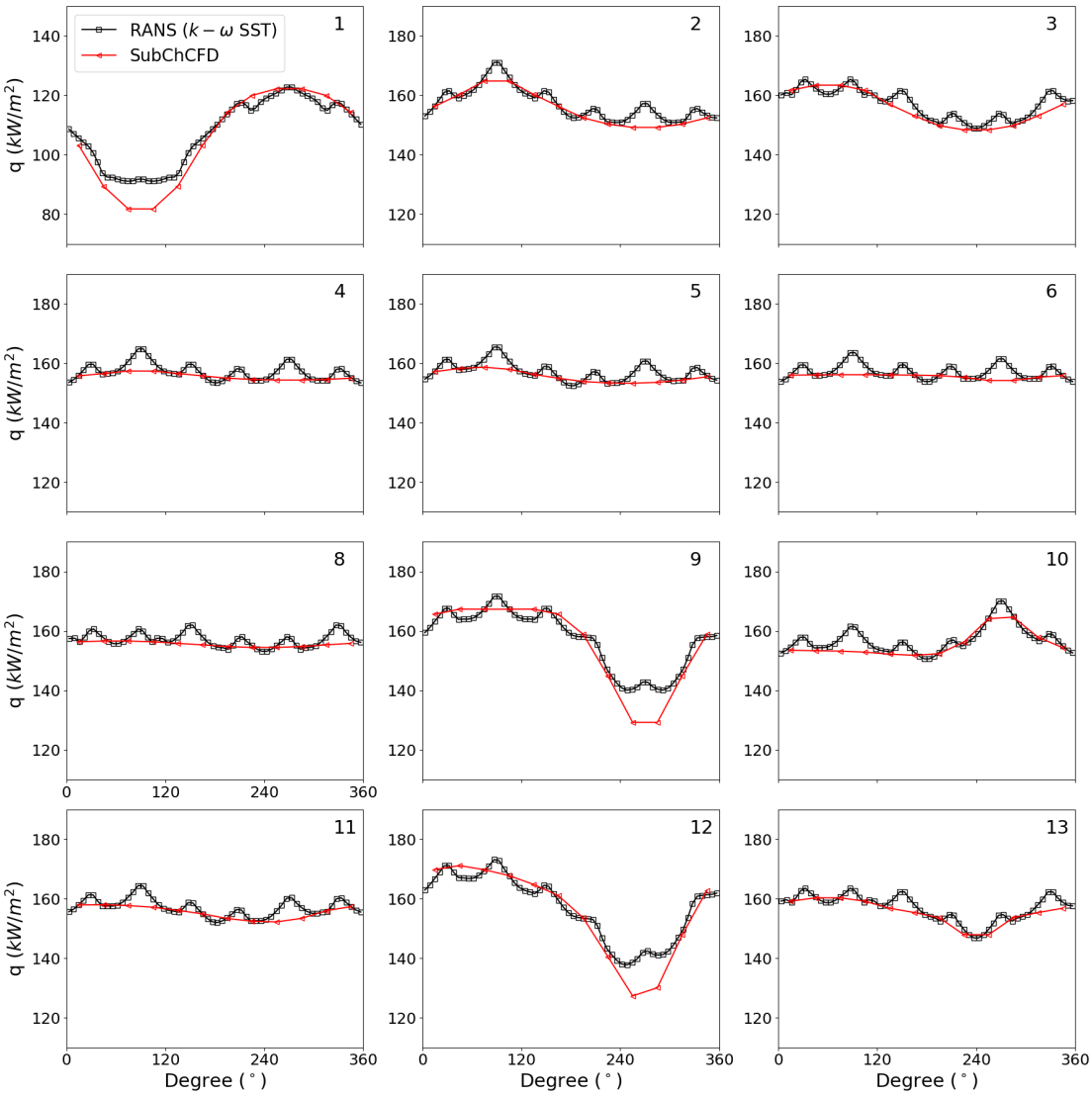

Figure 15: Circumferential distributions of the surface thermal fluxes of selected coolant channels.

Figure 16 shows the circumferential distributions of the surface temperature for the selected coolant channels. Once again, significant circumferential variations of the surface temperature appear in the centre and peripheral coolant channels, as a result of the large heat flux variations. The SubChCFD predictions closely align with those of the RANS model, although some

details are not fully captured. The biggest surface temperature differences within the coolant channels occur in channels 1, 9 and 12, reaching approximately 25°C. Given the inherently high temperatures in a HTGR core, even a 25°C difference could lead to a non-negligible radiative heat transfer within the coolant channels. It should be noted that such radiative heat transfer is not yet considered in the current study and will be the focus of further investigation in future work.

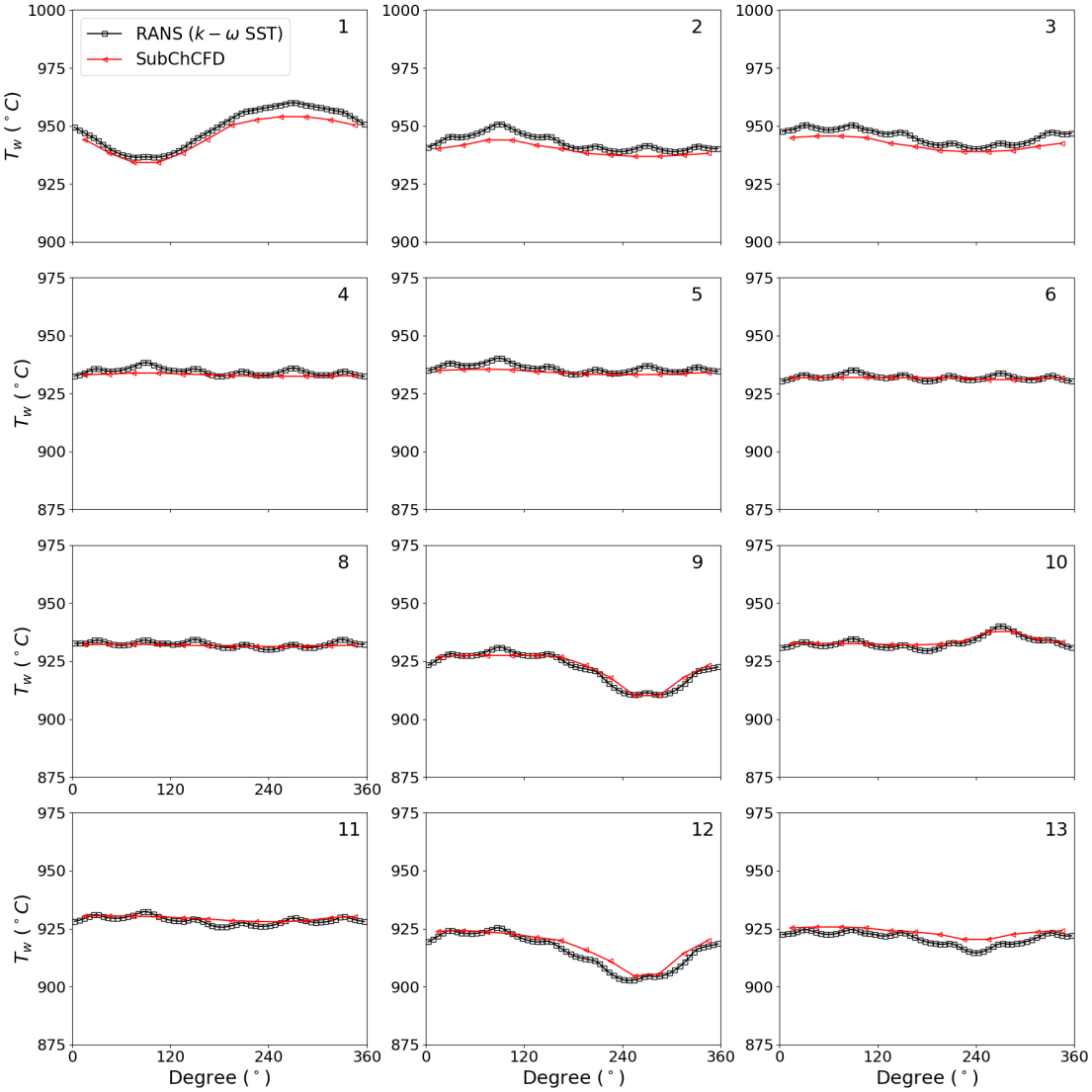

Figure 16: Circumferential distributions of the surface temperature of selected coolant channels.

Figures 17 and 18 show the temperature distributions over two lines: line 1 and line 2. Line 1 is a 60° inclined line connecting the left bottom corner to the centre of the fuel block, while Line 2 is a vertical symmetry line. There are five temperature peaks in line 1, corresponding to the five fuel compact regions, and three temperature troughs, corresponding to the three coolant channels. SubChCFD closely predicts coolant temperatures compared to the RANS model, even with only 6 to 7 grid points across each of the coolant channels. In contrast, the wall-resolved RANS model often requires very fine mesh distributions near the channel walls. Surprisingly, the most significant disagreement between SubChCFD and the RANS model occurs in the solid domain at the fuel regions near the centre of the fuel block, which is about 15 °C. On line 2, where no fuel regions, the five temperature troughs correspond to the five coolant

channels. It can be seen that the asymmetric features of the transverse coolant temperature distribution across the centre and peripheral channels are well captured by SubChCFD, giving an advantage of the method over the traditional unit cell approaches, where the coolant channel is often modelled in 1-D axially and 0-D transversely. The four temperature peaks correspond to the four gaps between the adjacent coolant channels. Again, the most significant disagreement between SubChCFD and the RANS model occurs in these regions, with a maximum temperature difference of approximately 8 °C.

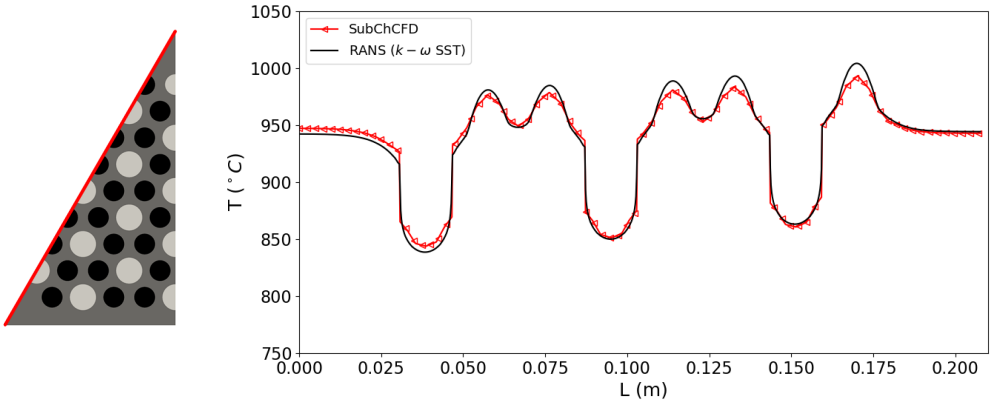

Figure 17: Temperature distribution over line 1.

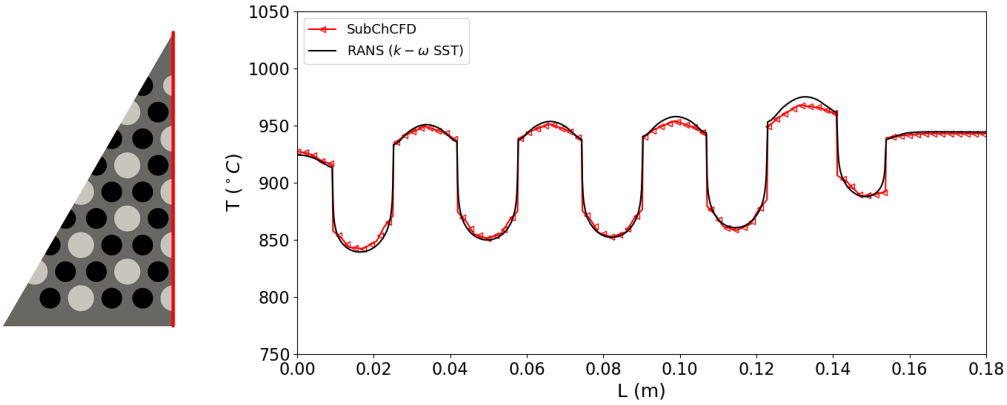

Figure 18: Temperature distribution over line 2.

3.2 Simulation of a full fuel assembly

Building upon the confidence gained from the aforementioned 2-D simulation, a 3-D simulation is carried out for a full-length MHTGR-350 fuel assembly to further validate the new functionality of SubChCFD. Table 1 provides some information about the fuel assembly. The assembly consists of 10 vertically stacked fuel blocks, each with a length of 0.793 m. Graphite plugs, 0.02 m long, are located at the two ends of each fuel block to enclose the fuel compacts. Consequently, the total length of the fuel assembly is 7.93 m, and the regions between the fuel blocks where graphite plugs are located do not generate heat. A uniform power density of 31.1 MW/m^3 is applied to the fuel compacts. The assembly mass flow rate is set at 2.6088 kg/s. Helium, entering at a temperature of 490 °C, flows through the assembly from top to bottom, and the expected mean outlet temperature is 950 °C.

Table 1: Description of the MHTGR-350 fuel assembly.

Parameter	**Value**
Length of an individual fuel block (m)	0.793
Length of the graphite plug (m)	0.02
Number of fuel blocks in the assembly	10
Fuel compact power density (MW/m^3)	31.1
Assembly mass flow rate (kg/s)	2.6088
Operating pressure (MPa)	7.0
Inlet helium temperature (°C)	490
Expected helium outlet temperature (°C)	∼950

With a substantial temperature increase of the helium gas along the flow direction, a strong flow acceleration is anticipated to happen due to density variation. This makes the assumption that the flow is not axially fully developed any more, hence necessitating 3-D modelling. Moreover, the varying thermal properties of the solid may influence heat transfer within the fuel assembly, leading to complex 3-D temperature distributions. In this study, the properties of the helium gas are tabulated at a temperature interval of 1 °C using the NIST database REFPROP v9 [10]. The properties of graphite and fuel compacts are derived from the work of Tak et al. [4] and Johnson et al. [11], and are re-fitted using fourth-order polynomials as given in Equation 13,

$$\Phi(T) = A_0 + A_1 T + A_2 T^2 + A_3 T^3 + A_4 T^4 \tag{13}$$

where Φ represents a specific physical property, A_0, A_1, ..., A_4 are coefficients of the polynomial. Tables 2 and 3 list the polynomial coefficients for the physical properties of the graphite H-451 and the fuel compact, respectively. It is important to note that these polynomials should not be used outside the temperature range of 300 °C to 1500 °C.

Table 2: Polynomial coefficients for the properties of graphite H-451.

Polynomial coefficient	ρ **[kg/m^3]**	Cp **[J/(kg·°C)]**	λ **[W/(m·°C)]**	
			300°C∼540°C	540°C∼1500°C
A_0	1.740E+03	-3.695E+02	2.897E+01	1.505E+02
A_1	-	4.890	-	-4.209E-01
A_2	-	-4.161E-03	-	5.192E-04
A_3	-	1.666E-06	-	-2.698E-07
A_4	-	-2.542E-10	-	5.182E-11

Table 3: Polynomial coefficients for the properties of fuel compact.

Polynomial coefficient	ρ **[kg/m^3]**	Cp **[J/(kg·°C)]**		λ **[W/(m·°C)]**
		300°C∼814°C	814°C∼1500°C	
A_0	2.390E+03	-3.629E+03	3.982E+02	4.779
A_1	-	1.873E+01	9.129E-01	-7.922E-04
A_2	-	-3.053E-02	-6.648E-04	5.186E-06
A_3	-	2.259E-05	2.308E-07	-2.564E-08
A_4	-	-6.310E-09	-3.043E-11	4.513E-13

Figure 19 shows the computational domain used in the 3-D SubChCFD model and provides a close-up view of the coarse mesh for an individual fuel block. Essentially, the 3-D mesh is constructed by extruding the 2-D mesh described in Section 2, covering the entire cross section of the fuel block. The mesh for the graphite plugs are created separately by directly changing the fuel zones into graphite in an extruded mesh to ensure a conformal interface when meshes are joined. It can be clearly seen that the coolant channels penetrates the entire length of the

fuel block, while the fuel compacts terminate at specific locations near the two ends where the graphite plugs are used to seal the fuels. The complete mesh for the fuel assembly is then created by combining the meshes of the stacked fuel blocks. The resulting mesh size is 9.4 million cells. As this work is focused on testing the new development of SubChCFD, the bypass and cross-flow gaps are not taken into account in the modelling for sake of simplicity.

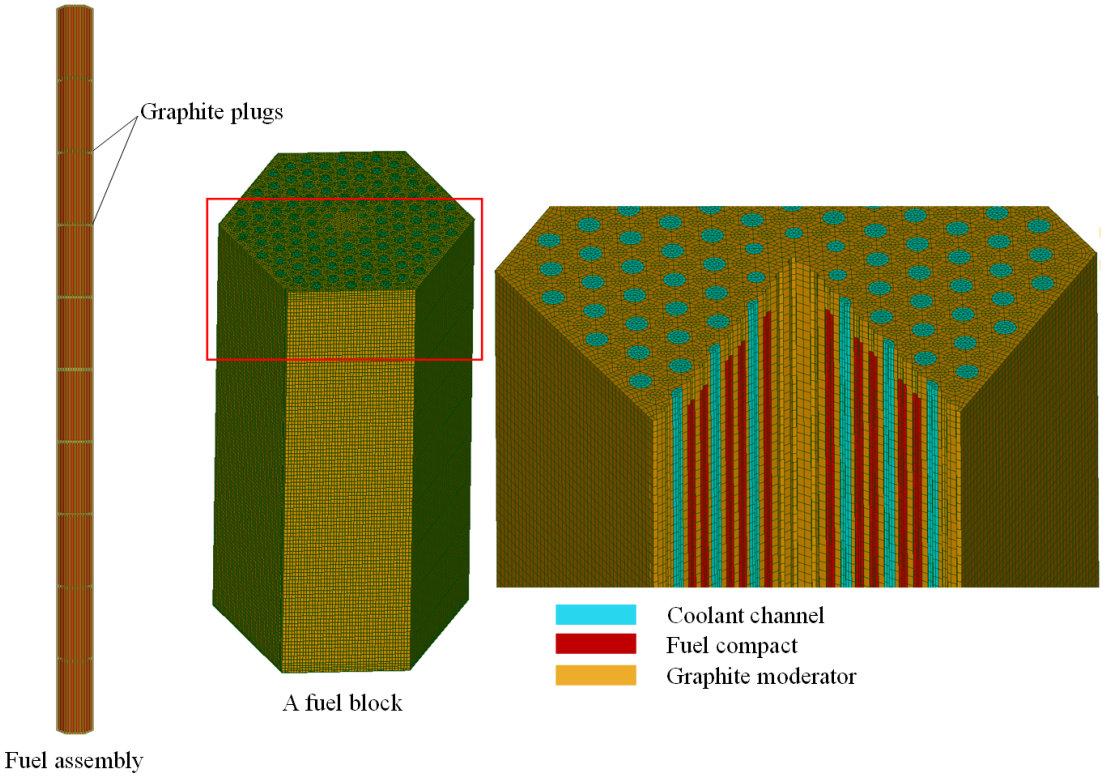

Figure 19: Computational domain and coarse-grid computing mesh for a full fuel assembly.

To validate SubChCFD, two RANS models are also created to provide reference results. In this case, a wall-modelled and a wall-resolved RANS models are used. To reduce computational cost, both RANS models are created based on the 1/12 sector of the fuel assembly. The k-ϵ turbulence model is used in conjunction with a wall function in the wall-modelled approach, and the mesh is created in line with this, resulting in a size of 33.4 million cells. In the wall-resolved model, the k-ω SST turbulence model is used, and the mesh is significantly refined in the near-wall regions of the coolant channels to ensure the first fluid cell to be placed within the viscous sublayer. The resulting mesh for the wall-resolved model consists of 97.1 million cells. Given that the RANS models are solely based on a 1/12 sector, the mesh size could be 40 to 120 times larger than that of SubChCFD for the same geometry, depending on the turbulence model and wall treatment approach used.

In both the SubChCFD and RANS models, symmetry boundary conditions are used for all lateral boundaries of the computational domain. As the distribution of velocity/mass flow among the coolant channel inlets (located at the top of the fuel assembly) cannot be determined a priori, a pressure boundary condition is used at the inlet to ensure a uniform head loss through the fuel assembly. A feedback mechanism is implemented to enable the imposed pressure value to self-adjust during the simulation, ensuring alignment with the prescribed target total mass flow rate. A standard pressure outlet boundary condition with a reference pressure of 7.0 MPa is applied to the coolant channel outlets.

The simulations are carried out on the UK's national High Performance Computing (HPC) system, ARCHER2. For SubChCFD, 2 nodes (providing 256 CPU cores) are used, while 24 nodes (providing 3,072 CPU cores) are used for the RANS models. Table 4 shows a rough

estimate of the computational cost, represented by CPU time per time step. Assuming that the parallel scalability in all simulations is linear, the CPU time can be calculated using Equation 14,

$$\text{CPU time} = \frac{\text{Elasped time} \times \text{Number of CPU cores}}{\text{Domain size}} \tag{14}$$

The CPU time per time step for SubChCFD is significantly lower, at 3.9×10^3 s, compared to the wall-modelled RANS, which is 571.4×10^3 s, and the wall-resolved RANS, which is considerably higher at $6{,}657.6\times10^3$ s. This implies that even the wall-modelled RANS is 140 times more computationally expensive than SubChCFD, let alone the wall-resolved RANS, which is 1,700 times more expensive in this particular case.

Table 4: Estimate of computational cost of the simulations.

	SubChCFD	**RANS (wall-modelled)**	**RANS (wall-resolved)**
Domain size	1	1/12	1/12
CPU cores used	256	3,072	3,072
Elapsed time per time step [s]	15.3	15.5	180.6
CPU time per time step [$\times10^3$s]	3.9	571.4	6,657.6

Figure 20 shows the pressure drop results for a selected coolant channel (channel 11, as depicted in Figure 12) within the fuel assembly. The pressure drop is not linear along the flow direction due to flow acceleration and the changing properties of the helium gas. This trend is predicted by SubChCFD and RANS models. However, the SubChCFD result indicates an overall higher pressure drop magnitude compared to the RANS predictions, while the latter two exhibit good agreement with each other. The observed difference is approximately 10%, larger than that observed in the 2-D case as shown in Figure 10, implying a potential degradation in the performance of the friction factor correlation when used for accelerating flows.

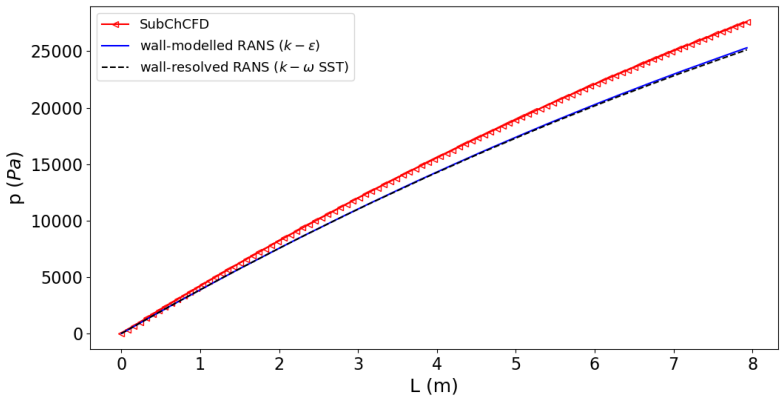

Figure 20: Pressure drop of channel 11.

Figure 21 shows the fluid temperature along the centreline of channel 11. Excellent agreement is observed among all three models. Since fluid temperature is significantly influenced by the mass flow distribution among coolant channels, the strong alignment in predictions implies that SubChCFD captures the same flow distribution as the RANS models, despite discrepancies in the pressure drop predictions of individual channels.

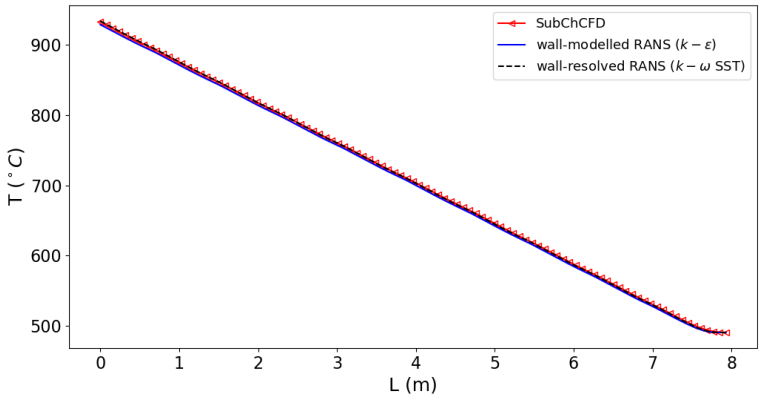

Figure 21: Axial distribution of the coolant temperature along the centreline of channel 11 in Figure 12.

Figure 22 shows the temperature distribution along the centreline of the fuel compact situated to the right of channel 11 (see Figure 12). As expected, the temperature exhibits a linear increase in the flow direction. The sharp temperature drop at the interface of the fuel blocks is a result of the presence of graphite plugs where no heating is generated. Again, the predictions from the two RANS models exhibit good agreement, and they are approximately 25 °C higher than the SubChCFD prediction. This suggests that the SubChCFD model predicts stronger heat transfer between the fuel and coolant, thereby bringing down the temperature difference between them. It is widely acknowledged that heat transfer impairment may occur due to partial laminarisation in accelerating flows with significant changes in physical properties. To account for such an effect, a correction to the Nusselt number correlation may be necessary. This will be explored further in the future work.

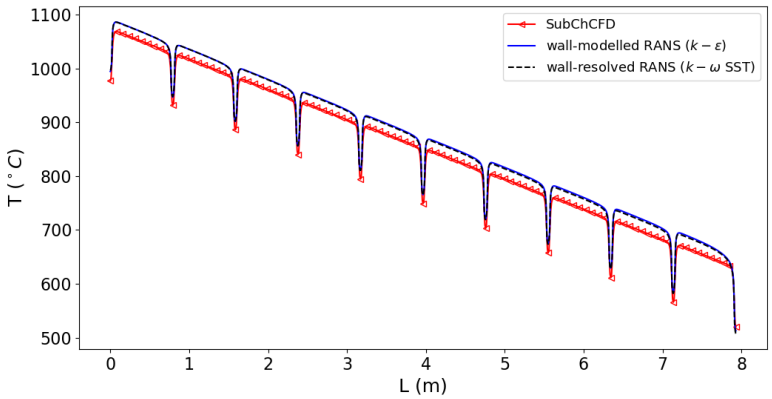

Figure 22: Axial distribution of the temperature along the centreline of the fuel rod situated to the right of channel 11 in Figure 12.

4 Conclusions

The main aim of this work is to extend a cost-effective coarse-grid approach SubChCFD, originally designed for light-water reactors, to prismatic HTGR fuel assemblies. To accomplish this, several new features are introduced into the exiting SubChCFD framework, including the ability to handle new geometries relevant to major prismatic HTGR fuel designs, the incorporation of new empirical correlations for closure modelling of the governing equations, and conjugated heat

transfer functionality, essential for modeling HTGR fuel assemblies. The new development is assessed through two test cases: a 2-D case for a fully developed flow and a full 3-D case based on practical HTGR design conditions. Both cases are centered around the General Atomics MHTGR-350 benchmark with multi-hole type of fuel elements.

SubChCFD exhibits excellent capabilities in simulating thermal-hydraulic phenomena under HTGR conditions, producing results of comparable quality to RANS approaches while employing a significantly coarser mesh. In the 3-D case, the computational cost of SubChCFD is estimated 140 times lower than that of a wall-modelled RANS model with wall-function approach and 1,700 times lower than that of a wall-resolved RANS model. Meanwhile, it is important to note that, when applied to problems involving substantial flow acceleration and property changes, as encountered in real HTGRs, discernible discrepancies can be observed between the SubChCFD and RANS CFD predictions. Specifically, a 10% discrepancy in assembly pressure drop and a maximum 25 °C difference in the fuel temperature are observed. These might be attributed to the empirical correlations used, as they are derived mostly based on fully developed flows. In the next step, implementation of corrections to these correlations to account for the effects of flow acceleration and property changes will be explored. Additionally, the thermal radiation will also be taken into account and their effects on temperature distribution will be investigated.

Acknowledgements

The present work is funded by EDF Energy R&D UK Centre. The authors would like to acknowledge the support received from the project lead Marc Chevalier and Ehimen Iyamabo, as well as the valuable discussions with them and other collaborators from the University of Sheffield and the University of Manchester. The authors also thank EPCC for providing HPC compute time through the ARCHER2 Pioneer project for passive cooling capabilities of HTGRs.

References

[1] BEIS, Advanced Modular Reactor Research, Development & Demonstration: Phase A, **2022**.

[2] B. Liu, S. He, C. Moulinec, J. Uribe, "Sub-channel CFD for nuclear fuel bundles", *Nuclear Engineering and Design* **2019**, *355*, 110318.

[3] Y. Fujiwara, M. Goto, K. Iigaki, T. Iyoku, H. Quan Ho, T. Kawamoto, M. Kondo, K. Kunitomi, K. Morita, S. Nagasumi, S. Nakagawa, T. Nishihara, N. Nojiri, M. Ono, A. Saikusa, N. Sakaba, T. Shibata, Y. Shimazaki, A. Shimizu, M. Shinozaki, J. Sumita, Y. Tachibana, S. Takada, D. Tochio, T. Uesaka, S. Ueta, *Design of High Temperature Engineering Test Reactor (HTTR)*, INC, **2021**.

[4] N. I. Tak, M. H. Kim, W. J. Lee, "Numerical investigation of a heat transfer within the prismatic fuel assembly of a very high temperature reactor", *Annals of Nuclear Energy* **2008**, *35*, 1892–1899.

[5] N. I. Tak, M. H. Kim, H. S. Lim, J. M. Noh, "A practical method for whole-core thermal analysis of a prismatic gas-cooled reactor", *Nuclear Technology* **2012**, *177*, 352–365.

[6] M. Ding, J. L. Kloosterman, "Thermal-hydraulic design and transient evaluation of a small long-life HTR", *Nuclear Engineering and Design* **2013**, *255*, 347–358.

[7] M. Nakano, N. Tsuji, Y. Tazawa, "Conceptual Reactor Design Study of Very High Temperature Reactor (VHTR) with Prismatic-Type Core", *Journal of Power and Energy Systems* **2008**, *2*, 768–774.

[8] B. Liu, S. He, C. Moulinec, J. Uribe, "A multiscale model of a rod bundle using subchannel CFD", *Nuclear Engineering and Design* **2022**, *393*, 111793.

[9] N. E. Todreas, M. S. Kazimi, *Nuclear Systems I: Thermal Hydraulic Fundamentals*, Taylor & Francis, **1990**, p. 384.

[10] E. W. Lemmon, M. L. Huber, M. O. McLinden, et al., "NIST standard reference database 23", *Reference fluid thermodynamic and transport properties (REFPROP) version* **2010**, *9*.

[11] R. W. Johnson, H. Sato, R. R. Schultz, CFD Analysis of Core Bypass Phenomena, tech. rep. November, Idaho National Laboratory, **2009**.